Mixing effects in the crystallization of supercooled quantum binary liquids

M. Kühnel, J. M. Fernández, F. Tramonto, G. Tejeda, E. Moreno, A. Kalinin, M. Nava, D. E. Galli, S. Montero, and R. E. Grisenti

Citation: The Journal of Chemical Physics **143**, 064504 (2015); doi: 10.1063/1.4928280
View online: http://dx.doi.org/10.1063/1.4928280
View Table of Contents: http://scitation.aip.org/content/aip/journal/jcp/143/6?ver=pdfcov
Published by the AIP Publishing

Mixing effects in the crystallization of supercooled quantum binary liquids

M. Kühnel,[1] J. M. Fernández,[2] F. Tramonto,[3] G. Tejeda,[2] E. Moreno,[2] A. Kalinin,[1]
M. Nava,[3,4] D. E. Galli,[3] S. Montero,[2] and R. E. Grisenti[1,5]
[1]*Institut für Kernphysik, J. W. Goethe-Universität, Max-von-Laue-Str. 1, 60438 Frankfurt am Main, Germany*
[2]*Laboratory of Molecular Fluid Dynamics, Instituto de Estructura de la Materia, CSIC, Serrano 121, 28006 Madrid, Spain*
[3]*Laboratorio di Calcolo Parallelo e di Simulazioni di Materia Condensata, Dipartimento di Fisica, Università degli Studi di Milano, Via Celoria 16, 20133 Milano, Italy*
[4]*Computational Science, Department of Chemistry and Applied Biosciences, ETH Zurich, USI Campus, Via Giuseppe Buffi 13, CH-6900 Lugano, Switzerland*
[5]*GSI - Helmholtzzentrum für Schwerionenforschung, Planckstr. 1, 64291 Darmstadt, Germany*

(Received 23 April 2015; accepted 28 July 2015; published online 11 August 2015)

By means of Raman spectroscopy of liquid microjets, we have investigated the crystallization process of supercooled quantum liquid mixtures composed of parahydrogen (pH_2) or orthodeuterium (oD_2) diluted with small amounts of neon. We show that the introduction of the Ne impurities affects the crystallization kinetics in terms of a significant reduction of the measured pH_2 and oD_2 crystal growth rates, similarly to what found in our previous work on supercooled pH_2-oD_2 liquid mixtures [Kühnel *et al.*, Phys. Rev. B **89**, 180201(R) (2014)]. Our experimental results, in combination with path-integral simulations of the supercooled liquid mixtures, suggest in particular a correlation between the measured growth rates and the ratio of the effective particle sizes originating from quantum delocalization effects. We further show that the crystalline structure of the mixtures is also affected to a large extent by the presence of the Ne impurities, which likely initiate the freezing process through the formation of Ne-rich crystallites. © *2015 AIP Publishing LLC.* [http://dx.doi.org/10.1063/1.4928280]

I. INTRODUCTION

The study of crystallization in supercooled liquids is of prime importance for understanding the fundamental mechanisms of crystal growth. It is relevant to diverse research areas such as microstructural control in alloys engineering or the formation of ice in the atmosphere. In addition, it is of increasing interest in the context of the glass transition,[1] as the maximum rates of crystal growth may themselves provide insights into the glass-forming ability of supercooled liquids.[2–5] Among the systems that can be used as test beds for our current microscopic understanding of crystallization in supercooled liquids are binary mixtures. The crystallization of binary mixtures differs significantly from that of pure fluids, displaying a rich phase behavior in dependence of particle size ratio and composition. For example, understanding why for some compositions certain metallic binary alloys invariably form crystal phases that compete with the glass formation[6] is an open and fundamental question for understanding crystallization and its interplay with the glass-forming ability.

The dynamics and crystallization of supercooled liquid binary mixtures in dependence on composition and particle size disparity have been investigated by classical molecular dynamics simulations of systems interacting through a simple Lennard-Jones (LJ) pair potential.[7–10] However, systematic experimental studies of such simple atomic and molecular systems have so far remained out of reach. Here, we present experimental results, obtained by employing the liquid microjet technique in combination with Raman light scattering,[11] on the crystallization process of supercooled binary liquid mixtures of either pH_2 or oD_2 diluted with small amounts of Ne impurities.

The present work was partly motivated by our recent investigations of the crystallization kinetics in supercooled pH_2-oD_2 liquid mixtures.[12] The most striking observation in those studies was the strong dependence of the crystallization rate on composition: starting with a pure pH_2 system, the crystal growth was found to slow down considerably with increasing amount of oD_2, reaching a maximum in the crystallization time at about 20% oD_2 content. This behavior may appear surprising because the intermolecular interaction potential is isotope independent.[13] However, quantum delocalization due to zero-point motion increases the radius of the pH_2 and oD_2 molecules to a different extent due to their different masses, resulting in an effective oD_2 to pH_2 particle size ratio smaller than unity. The observed slowdown of crystal growth in these quantum binary mixtures appears thus to be governed by an interplay between composition *and* particle size disparity that is in many respects similar to that found in simulations of classical binary mixtures.[14]

Here, we have extended the above studies to supercooled pH_2-Ne and oD_2-Ne liquid mixtures, addressing also relevant structural aspects of the crystallization process in the Ne mixtures, as well as in diluted pH_2-oD_2 mixtures, which have been not taken into account in our recent work.[12] In principle, a Ne atom can be viewed as an isotopic impurity when mixed to pH_2 or oD_2 because its interatomic spherical potential is very similar to those of pH_2 and oD_2. Indeed, the LJ potential parameters (potential well depth ϵ and interaction length σ) for the H_2–H_2 interaction are σ = 2.96 Å and ϵ = 34.2 K,

while for H_2–Ne, they are $\sigma = 2.8745$ Å and $\epsilon = 35.49$ K (Ref. 15). However, Ne is 10 times heavier than pH_2 and, as a consequence, the magnitude of quantum delocalization is much smaller, resulting in a significantly smaller effective size when compared to pH_2 or oD_2. The pH_2-Ne and oD_2-Ne liquid mixtures investigated here represent thus ideal systems to further explore the effect of composition and particle size ratio on the crystallization of supercooled binary liquid mixtures.

II. EXPERIMENTAL DETAILS

The supercooled liquid mixtures were produced by the microjet technique and probed by Raman scattering, as described in Refs. 11 and 16. A schematic view of the experimental setup is shown in Fig. 1. The liquid jet, which propagates at a speed $v \simeq \sqrt{2P_0/\rho}$ (P_0 is the source pressure and ρ is the liquid density), rapidly cools well below the melting temperature until it crystallizes, producing a continuous solid filament several cm long.[11] A crucial feature of our approach is represented by the correspondence between the distance along the jet propagation direction, z, and time, $t = z/v$, allowing for a probe of the crystallization kinetics with sub-microsecond time resolution.

The liquid mixtures were continuously injected into vacuum through a 5 μm-diameter glass capillary nozzle. The glass capillary, mounted on a microactuators stage allowing a displacement of the entire nozzle assembly, and thus of the probed volume (Fig. 1), along the x, y, and z directions with an accuracy of better than 1 μm, was cooled by a continuous flow liquid helium cryostat, and its temperature T_0 was actively stabilized within ±0.1 K. The vacuum chamber was evacuated by a 2000 l/s turbo molecular pump providing a background pressure below 3×10^{-3} mbars. The nuclear spin variants pH_2 and oD_2 in the $J = 0$ rotational state were produced by continuous catalytic conversion at 17 and 22 K, respectively, from 99.9999% and 99.9% purity natural H_2 and D_2 gases, respectively, resulting in 99.8% and 97.5% purity pH_2 and oD_2, respectively, the rest being represented by odd-J molecules.

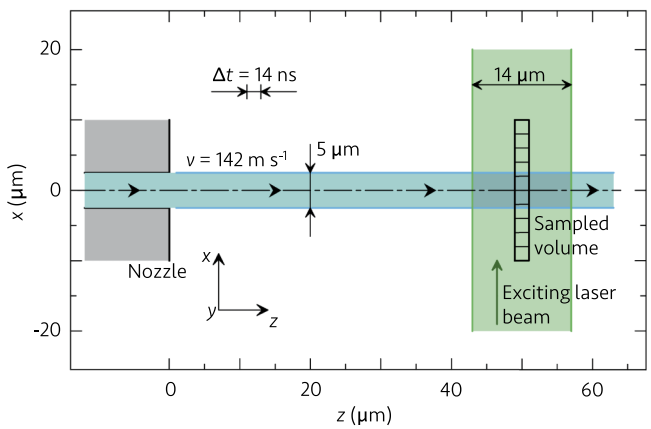

FIG. 1. Schematic view of the experiment, drawn to scale. The liquid microjet (light blue) flows along the z axis. The exciting laser beam (green) polarized parallel to either the z or y axes propagates along the x direction. Raman scattering is collected along the y direction. The depicted sampled volume is the projection, onto the scattering plane, of the spectrograph entrance slit and of the active area of the CCD detector, showing the space resolution.

The room temperature gas streams of pH_2, oD_2, and 99.998% purity Ne were then mixed at the specific ratios by two mass flow controllers, one for each component, working at a minimum flow rate of 20 normal-ml/min. The equilibrium solubility of neon in hydrogen in the liquid phase is limited to about 5%, and to about twice that value for neon in deuterium, whereas a phase separation occurs at higher Ne content.[17–20] The experimental conditions for all the mixtures investigated here are reported in Table I.

The liquid microjets were probed by recording Raman spectra of the vibrational $Q_1(0)$ and rotational $S_0(0)$ transitions of pH_2 and oD_2 as a function of z. The Ne impurities could not be detected as they are Raman scattering inactive. Raman scattering was excited by a 4 W plane-polarized cw Ar^+ laser beam at $\lambda = 514.5$ nm, with an intracavity etalon for single-mode operation, and focused down to a diameter of ≈14 μm onto the filament. The polarization plane of the exciting laser beam could be rotated by means of a $\lambda/2$ plate at the exit of the laser cavity. During the measurements of the rotational spectra, the exciting laser beam was polarized along the y axis (Fig. 1) in order to minimize the stray light resulting from the elastic scattering, whereas for the vibrational spectra, it was polarized along the z axis to record the Raman scattering in full.

The Raman signal, which is proportional to the molecular number density, was collected at 90° with respect to both the laser beam and filament axis and was focused onto the 20 μm entrance slit of the spectrometer by an optical system with ×9 magnification. A supernotch filter was used to block part of the very intense Rayleigh scattering from the liquid filament. The spectrometer, with one meter focal length, was equipped with a 2360 groove/mm grating and a back-illuminated CCD detector with 20×20 μm^2 pixels cooled by liquid nitrogen to 153 K. Its spectral resolution is ≈0.11 cm^{-1} at 4150 cm^{-1} (pH_2 vibrational band) and ≈0.24 cm^{-1} at 180 cm^{-1} (oD_2 rotational band). As illustrated in Fig. 1, the space resolution along the jet axis was determined by the ≈2 μm projection of the spectrograph slit onto the microjet. Along the x radial direction, 10 stripes, each 2 pixels high, were read onto the CCD detector, allowing for a radial sampling of the jet. The Raman spectra presented here were obtained by adding up just over the illuminated stripes.

TABLE I. Relevant experimental parameters (see the text for details) and impurity content for all the systems studied in the present work.

System	Impurity	(mol. %)	P_0 (bar)	T_0 (K)	v (m/s)
pH_2	...	0	8.5	16.0	142
oD_2	...	0	13.0	19.6	115
	Ne	0.3	9.4	17.0	147
pH_2-Ne	Ne	1	11.2	17.5	153
	Ne	2	10.8	18.0	137
	Ne	1	16.0	20.0	125
oD_2-Ne	Ne	2	17.0	20.0	123
	Ne	5	11.8	20.0	95
	oD_2	1	11.5	16.0	164
	oD_2	3.2	8.9	16.0	143
pH_2-oD_2	oD_2	4.6	9.3	16.0	144
	pH_2	2.4	16.3	20.0	130
	pH_2	4.3	15.3	20.0	127

III. RESULTS

A. Crystallization kinetics

Examples of vibrational spectra for oD_2-Ne and pH_2-Ne mixtures containing 1% Ne are shown in Figs. 2(a) and 2(b), respectively, evidencing the phase transition from the liquid to the solid. As mentioned above, the crystallization behavior of the Ne impurities could not be addressed during the present work because they are not Raman active. The vibrational spectra allow extracting the solidified fraction of the sampled filament volume. The evolution of the oD_2 and pH_2 solid fractions measured for all the oD_2-Ne and pH_2-Ne mixtures investigated in the present work are shown in Figs. 2(c) and 2(d), respectively, where the axial distance has been converted into time as explained above.

We see in Fig. 2(d) that the presence of merely 1% Ne atoms results in a significantly earlier start of crystallization compared to pure pH_2, with the vibrational peak corresponding to solid pH_2 appearing already within the first 100 μm distance from the orifice [Fig. 2(b)], whereas the solidification process lasts about twice with respect to the pure pH_2 case. In the case of the oD_2-Ne mixtures [Fig. 2(c)], the presence of up to 2% Ne does not actually lead to a clear earlier onset of freezing with respect to the pure case, though the subsequent crystal growth slows down with increasing Ne concentration in a similar fashion as for the pH_2-Ne mixtures. Overall, the crystallization kinetics features seen in Fig. 2 are qualitatively similar to those reported recently for pH_2-oD_2 mixtures,[12] yet both the slowdown of crystal growth and the earlier onset of freezing upon mixing appear here strongly enhanced.

B. Crystal structure

The vibrational Raman spectra provide insights into the crystallization kinetics but they do not offer any straightforward information on the structure of the growing crystal. Such information can be retrieved from the rotational spectra, which we have measured for the pH_2-Ne and oD_2-Ne mixtures, as well as for diluted pH_2-oD_2 mixtures. Since the rotational spectrum of the liquid is a broad band in all cases, we focused here on the structural properties after completion of the freezing process. The evolution of the rotational excitations during the liquid-to-solid phase transition in supercooled pH_2 has been discussed elsewhere.[11]

In Figs. 3(a) and 3(b), we present the rotational spectra measured for the pH_2-oD_2 mixtures with oD_2 and pH_2 as impurity, respectively; the spectra were recorded at a distance of about 4 mm downstream from the orifice, corresponding to a propagation time of 40 μs, long enough for a complete crystallization in all cases (see Fig. 2). The rotational bands of the pure solid pH_2 [Fig. 3(a)] and oD_2 [Fig. 3(b)] filaments are characterized by four distinct peaks. This feature has been attributed to a random hexagonal closed packed (rhcp)

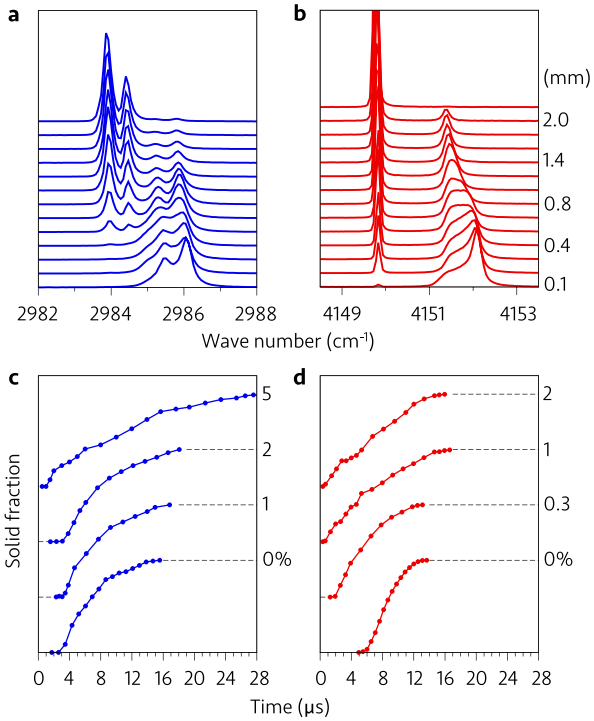

FIG. 2. Selected normalized vibrational Raman spectra of (a) oD_2 and (b) pH_2 measured as a function of the distance z from the orifice (right scale) for the 1% Ne mixtures. The double-line shape of the oD_2 bands visible in (a) results from the presence of less than 3% of $J = 1$ pD_2 molecules, with a 50-fold enhancement in the Raman scattering intensity with respect to the $J = 0$ molecules.[21] Panels (c) and (d) show the time evolution of the solid fractions extracted from the vibrational bands for oD_2 and pH_2, respectively, in mixtures with mole percentages indicated on the right axis. The solid fractions range from 0 to 1, as indicated by the dashed lines on the left and on the right of the experimental curves, respectively.

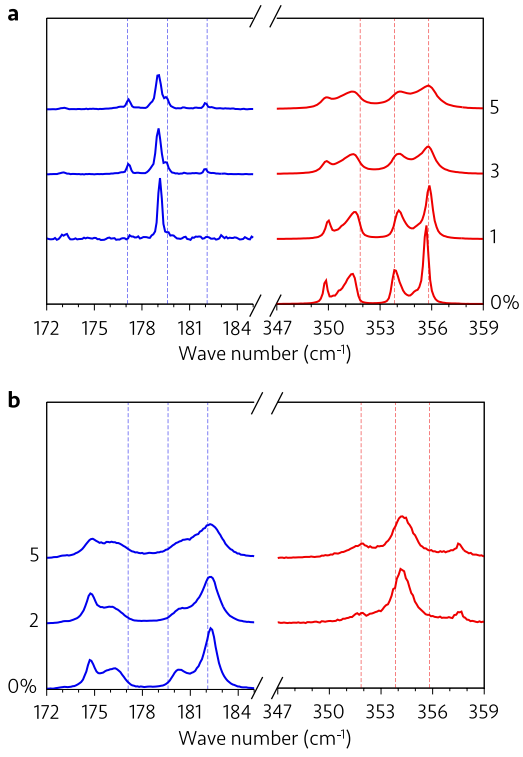

FIG. 3. Normalized rotational Raman spectra of oD_2 (blue) and pH_2 (red) in completely solidified filaments of diluted pH_2-oD_2 mixtures. The impurity component is oD_2 and pH_2 in (a) and (b), respectively. The oD_2 and pH_2 impurity percentages are indicated on the right and left scales in (a) and (b), respectively. Vertical red and blue dashed lines indicate the position of the Raman lines measured for equilibrium hcp crystals of pure pH_2 and oD_2, respectively. The small peaks visible around 173 cm^{-1} in (a) and around 358 cm^{-1} in (b) are plasma lines from the Ar^+ laser.

structure, i.e., an alternating stacking of hexagonal closed-packed (hcp) and face-centered cubic (fcc) crystal domains.[11] In fact, bulk solid pH_2 and oD_2 slowly grown from the melt always exhibit a hcp structure, whose rotational Raman spectrum consists of three lines [the red and blue dashed lines in Figs. 3(a) and 3(b), respectively]. However, while the hcp lattice is the most stable crystal structure, it was experimentally found that bulk solid pH_2 and oD_2 grown fast from the vapor at very low temperatures also form the fcc crystal lattice, which differs in energy from the hcp lattice only by a factor of $\sim 10^{-5}$ (Ref. 13). The rotational Raman band of the pH_2 fcc structure consists of two peaks at ≈ 350 cm^{-1} and ≈ 356 cm^{-1}, the latter overlapping with one peak corresponding to the hcp structure. The addition of small amounts of the impurity leads to a broadening of the rotational features, as shown in Figs. 3(a) and 3(b), while maintaining the coexistence of the hcp and fcc lattices. This broadening of the rotational lines upon dilution with either oD_2 or pH_2 has been observed and interpreted previously as the result of the coupling between the rotational states in the solid mixtures.[21]

Turning now to the analysis of the rotational excitations relative to the impurity, some striking features appear. For instance, we see in Fig. 3(a) that at the lowest concentration of 1% oD_2, the oD_2 rotational spectrum exhibits a single line at ≈ 179 cm^{-1}. This line is very sharp and its wave number and width match those of the gas phase. This suggests that most of the oD_2 impurities occupy sites with no nearest neighbor oD_2 molecules, being able to rotate freely as a results of the larger average distance between the pH_2 molecules in the crystal matrix. With increasing oD_2 impurity concentration up to about 5%, we observe the gradual appearance of three additional sharp lines at the wave numbers of the oD_2 bulk hcp crystal lattice.[13] This can be rationalized in terms of nearest neighbor $(oD_2)_2$ pairs surrounded by pH_2 molecules, where the magnetic degeneracy of the rotational states is split along the intermolecular axis, giving rise to the hcp triplet.[22]

In the case of pH_2-oD_2 mixtures with pH_2 as impurity [Fig. 3(b)], we find a similar trend, yet with noticeable differences. The pH_2 rotational spectrum at the lowest concentration of 2% pH_2 is also characterized by a main peak whose wave number agrees with that of the free molecule, indicating that most of the pH_2 molecules are surrounded by oD_2 nearest neighbors. However, this Lorentz-shaped peak is significantly broader than in the case of isolated oD_2 impurities [Fig. 3(a)] because the broader zero-point wave function of a pH_2 molecule explores part of the repulsive potential of surrounding oD_2 molecules, affecting its rotational motion and thus giving rise to a broader Raman peak. The small side peak at ≈ 352 cm^{-1}, which grows with increasing pH_2 concentration, matches the lowest-energy excitation line of the hcp triplet in the bulk (red dashed lines). This suggests again that a fraction of the pH_2 molecules in the lattice is arranged in nearest neighbor $(pH_2)_2$ pairs, the remaining two hcp peaks being probably hidden by the broad central peak.

The rotational spectra of the solidified filaments containing Ne as impurity are presented in Fig. 4, evidencing remarkable differences with respect to the case of the pH_2-oD_2 mixtures. In Fig. 4(b), we can see that the intensities of the hcp lines of pH_2 at $\simeq 353$ and $\simeq 356$ cm^{-1}, for a Ne concentration

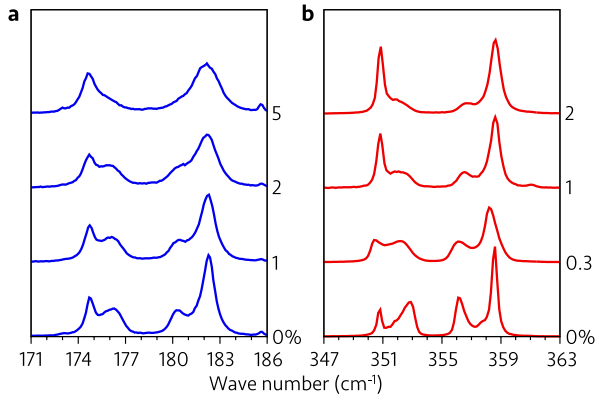

FIG. 4. Normalized rotational Raman spectra of (a) oD_2 and (b) pH_2 in completely solidified filaments of diluted oD_2-Ne and pH_2-Ne mixtures, respectively. The Ne impurity content is indicated on the right scale.

as low as 0.3%, drop to approximately half of their value for pure pH_2 and become vanishingly small for the 2% Ne mixture. Simultaneously, the intensity of the fcc line at 351 cm^{-1} increases, becoming the dominant feature, together with the line at 359 cm^{-1}, at the highest Ne concentration of 2%. A similar trend is observed for the oD_2-Ne mixtures [Fig. 4(a)], though the two dominant peaks at $\simeq 175$ and $\simeq 182$ cm^{-1} in the oD_2 rotational spectra at the highest Ne concentrations are broader than those in the pH_2 spectra of Fig. 4(b). Overall, the data of Fig. 4 indicate that by adding small amounts of Ne to either pH_2 or oD_2, the crystal structure changes from a rhcp configuration to a dominant fcc structure, which is the equilibrium configuration of solid neon. We point out that the slow crystallization from equilibrium H_2-Ne and D_2-Ne liquid mixtures results in a physical separation into pure Ne and H_2 (D_2) solid phases, where the amount of the fcc domains is negligibly small at such low Ne concentrations.[18–20]

IV. DISCUSSION

At the microscopic scale, the process of solidification from the melt is governed by crystal nucleation and the subsequent crystal growth. The overall picture that emerges from our crystallization data is that the inclusion of a small amount of impurity atoms reduces, on one side, the time required for the formation of a critical crystallite and, on the other side, slows down the subsequent crystal growth. The reduced nucleation time, which has been previously observed in pH_2-oD_2 mixtures,[12] can be now understood qualitatively with the aid of the rotational Raman spectra. In fact, we have seen (Fig. 4) that the presence of Ne impurities tends to force both pH_2 and oD_2 to crystallize into a fcc lattice, which is the equilibrium structure of solid Ne. It is unlikely that the presence of $\sim 1\%$ of Ne impurities, randomly distributed in the lattice, would be able to modify the host pH_2 or oD_2 crystal structure to such an extent. Thus, the immediate interpretation of these observations is that the Ne impurities trigger the crystallization process with the formation of Ne-rich fcc crystallites that subsequently grow into the surrounding pH_2- or oD_2-rich supercooled liquid by keeping their initial crystal structure. The formation of Ne-rich nucleation sites is probably driven by a combination of compositional fluctuations and deep supercooling. Since the

probability for the formation of large Ne clusters increases with increasing impurity amount, the above simple picture would thus explain the earlier start of crystallization upon addition of Ne impurities. We also note that the growth of pH_2 and oD_2 into a fcc structure can be facilitated by the small energy difference between the fcc and hcp lattices.[13] Such a clear tendency to assume a specific crystal structure is not seen in the pH_2-oD_2 mixtures (Fig. 3), likely due to the fact that both pH_2 and oD_2 crystallize into a hcp lattice.[13] The slight differences in the occurrence of the onset of freezing in the pH_2-Ne and oD_2-Ne mixtures [compare Figs. 2(d) and 2(c)] may be partly related to the equilibrium D_2-Ne phase diagram,[20] which shows a slight decrease of the liquidus temperature at small (<3%) Ne concentrations, in stark contrast to its increase observed in equilibrium H_2-Ne mixtures.[17,18]

For a discussion of the crystallization kinetics, we present in Fig. 5 a summary of the growth rate data by plotting the total crystallization time of the solvent (either pH_2 or oD_2), relative to the pure case, as a function of the impurity content for the pH_2-Ne and oD_2-Ne mixtures, as well for the pH_2-oD_2 mixtures.[12] One can distinguish two limiting cases, represented on one side by the barely significant increase of the crystallization rate of oD_2 upon dilution with pH_2 (red squares) and, on the other side, by the strong dependence on the Ne impurity content of the crystallization rate of pH_2 (green circles).

According to the classical kinetic theory,[23] the crystal growth rate is expressed in terms of thermodynamic and kinetic factors as

$$u(T) = k(T)\left[1 - e^{-\Delta G(T)/k_B T}\right], \quad (1)$$

where T is the temperature, $\Delta G(T)$ is the difference in Gibbs free energy (per molecule) of the liquid and the crystal and is therefore the driving force for crystallization, $k(T)$ is the crystal deposition rate at the liquid-crystal interface, and k_B is Boltzmann's constant. For the isotopic pH_2-oD_2 mixtures, $\Delta G(T)$ can be computed from the experimental heat capacity data for the pure pH_2 and oD_2 systems, and just a slight dependence on composition was found.[12] Due to the lack of experimental heat capacity data, a similar direct determination of $\Delta G(T)$ was not possible for mixtures containing Ne. However, due to their nearly isotopic nature, we do not expect that the thermodynamic factor plays a major role when describing the crystallization kinetics of pH_2-Ne and oD_2-Ne mixtures. Accordingly, the observed composition dependence of the crystal growth rate must be contained in the kinetic term $k(T)$. The empirical Wilson-Frenkel model assumes that crystal growth is an activated process in which mass transport, expressed in $k(T)$ through the diffusion constant, represents the most important limiting factor for the growth rate.[23] But how does mixing affect the transport properties, and consequently the growth rate, to the extent reported here? A number of simulation studies proposed that a lower particle diffusivity can be associated with packing effects resulting from the development in the liquid of some local structural ordering.[24] Recently, the composition dependence of transport properties observed in experiments with binary metallic alloys has been explicitly linked to corresponding changes in the density of packing.[25,26] Indeed, from a pure geometrical point of view, the packing efficiency in a mixture of hard spheres of specific size ratio is a function of composition.[27]

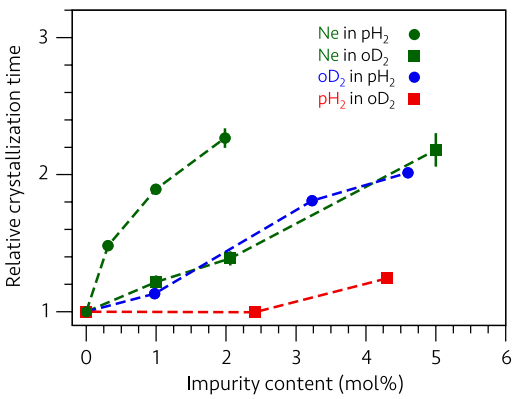

FIG. 5. Crystallization time for microjets of diluted pH_2-Ne and oD_2-Ne liquid mixtures as determined from the pH_2 (green circles) and oD_2 (green squares) solid fraction curves of Figs. 2(d) and 2(c), respectively. Also shown are our previous data obtained for pH_2-oD_2 mixtures[12] with oD_2 (blue circles) and pH_2 (red squares) as the impurity species. The plotted data indicate relative values with respect to the crystallization time measured for either pure pH_2 (≈8 μs) or pure oD_2 liquid jets (≈13 μs). The dashed lines are guides to the eye.

In this regard, path integral Monte Carlo (PIMC) simulations of supercooled pH_2-oD_2 liquid mixtures[12] have revealed that the difference in the effective sizes associated with the pH_2 and oD_2 isotopes translates into a higher degree of icosahedral-like order around an oD_2 molecule than around a pH_2 molecule. Among the possible local geometrical structures, icosahedra are those that are most densely packed and have been associated in the literature with the glass-forming ability of supercooled liquids.[28] We have performed analogous PIMC simulations of the Ne mixtures, see the Appendix for details; we wish to emphasize that the PIMC simulations are only able to provide insights into the static properties of the disordered supercooled liquid phase.

In Fig. 6, we plot the partial radial pair distribution functions $g(r)$, which represent the average static inter-particle correlations, computed for pH_2-Ne and oD_2-Ne mixtures with 3% Ne content. The functions $g(r)$ not only confirm that, because of its larger mass, a Ne atom exhibits a significantly smaller effective size than that associated with the pH_2 and oD_2 molecules but they also allow us establishing a suggestive trend: the degree of the observed slowdown of crystal growth upon mixing is roughly correlated with the ratio of the effective sizes of the impurity and solvent particles for that specific mixture. In fact, one can obtain an indirect estimation of the effective particle size ratio by comparing the first peak positions in the corresponding partial pair distribution functions. For the pH_2-Ne mixture, which exhibits the strongest decrease in the rate of crystal growth with increasing impurity content (Fig. 5), the ratio of the first peak positions in the $g_{pH_2-Ne}(r)$ and $g_{pH_2-pH_2}(r)$ functions results to be ≈0.966; for the oD_2-Ne mixture, the ratio of the first peak positions in $g_{oD_2-Ne}(r)$ and $g_{oD_2-oD_2}(r)$ increases to about 0.971. For the pH_2-oD_2 mixtures investigated in Ref. 12, we have estimated an effective particle size ratio of ≈0.993 and ≈1.014 with oD_2 and pH_2 as the impurity, respectively.

In Fig. 7, we plot the probability distributions for icosahedral-like order obtained by a local bond order (LBO)

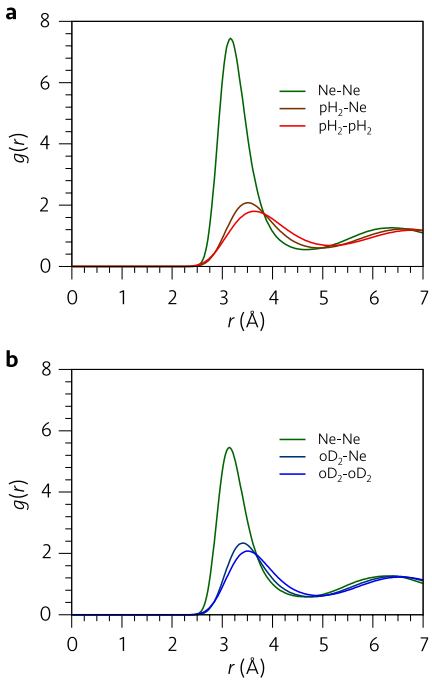

FIG. 6. Partial radial distribution functions $g(r)$, representing the three pair correlations, computed along the PIMC simulations of (a) pH_2-Ne and (b) oD_2-Ne mixtures with 3% Ne at $T = 13$ K and $T = 17$ K, respectively.

analysis of the particle configurations (see the Appendix). We see that, as a result of the larger Ne mass compared to oD_2, the tendency to a higher degree of icosahedral-like order around a Ne impurity in the pH_2-Ne mixtures is more pronounced than that found around an oD_2 molecule in pH_2-oD_2 mixtures.[12] In addition, the comparison in Fig. 7 of the distributions computed for the pH_2-Ne and oD_2-Ne mixtures shows that the probability for local ordering around a Ne impurity in the former mixture is appreciably higher than in the latter mixture. These results seem thus to further support the idea of a connection between liquid structural ordering and slower crystal growth, yet establishing the microscopic mechanisms of this dependence remains a formidable task.[24] Recent

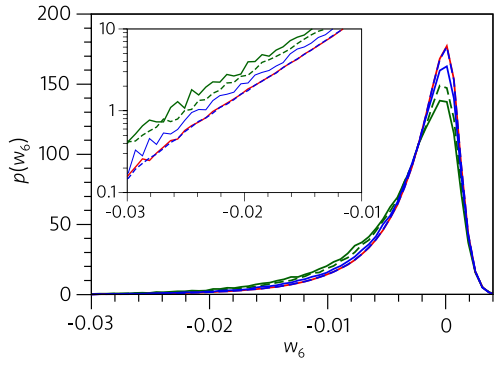

FIG. 7. Probability distribution $p(w_6)$ for icosahedral-like order for the pH_2 (red), oD_2 (blue), and Ne (green) particles computed for the same conditions as in Fig. 6. The inset shows an enlarged view of the tail on a logarithmic scale. The green solid and dashed lines refer to the pH_2-Ne and oD_2-Ne mixtures, respectively, whereas the blue solid line is the distribution relative to the pH_2-oD_2 mixture with 3% oD_2 computed in Ref. 12. Note the similar probabilities for local icosahedral packing around a pH_2 or oD_2 molecule (red solid and blue dashed lines, respectively) in the 3% Ne mixtures.

molecular dynamics simulation studies of crystal growth in supercooled binary alloys have demonstrated the importance of structural ordering in the liquid near the liquid-crystal interface in determining the crystal growth rate.[4,29] The extent to which such findings could be relevant to the interpretation of the effects of mixing reported here for quantum binary mixtures represents, however, an open and interesting question that deserves further work. As a final comment, we note that a possible competition between the hcp and fcc structures, as suggested by our experimental data (see Fig. 4), might also contribute to the slowdown of crystal growth in the pH_2-Ne and oD_2-Ne mixtures; the frustration of the crystallization due to the conflict between different crystalline structures is a possibility that has been discussed in the context of simulation studies of classical binary mixtures.[9,10]

To conclude, we have shown that the combination of liquid microjets and Raman light scattering can provide highly valuable information on the crystallization process in supercooled quantum binary liquid mixtures. Our results indicate in particular that effects related to effective particle size disparity originating from quantum delocalization must be considered when deepening our understanding of crystal growth in these quantum systems. From the experimental side, it would be highly desirable that the present results could be complemented by exploiting the capabilities offered by the liquid microjet technique in combination with state-of-the-art X-ray sources. Such studies would have the potential to shed further light on the physical origin of the findings reported here and thus on the basic mechanisms of crystal growth.

ACKNOWLEDGMENTS

We acknowledge financial support by the Deutsche Forschungsgemeinschaft, through Grant No. 593962, and the Spanish Ministerio de Ciencia e Innovación, through Grant Nos. FIS2010-22064-C02 and FIS2013-48275-C2. We acknowledge CINECA and the Regione Lombardia award, under the LISA initiative, for the availability of high performance computing resources and support.

APPENDIX: SIMULATION DETAILS

We have simulated pH_2-Ne and oD_2-Ne mixtures with 3% Ne by assuming a simple LJ pair potential to model the interaction among the Ne atoms,[15] the standard Silvera-Goldman potential[30] to model the interaction among hydrogen molecules, and the pair potential reported in Ref. 15 to model the pH_2–Ne and oD_2–Ne interactions. We have simulated systems with $N = 300$ particles in boxes with periodic boundary conditions at a density given by the linear relation $\rho = 0.97\rho_{pH_2,oD_2} + 0.03\rho_{Ne}$, where $\rho_{pH_2} = 0.0232$ Å^{-3}, $\rho_{oD_2} = 0.0263$ Å^{-3}, and $\rho_{Ne} = 0.0373$ Å^{-3} are the densities close to triple-point conditions of the pure substances.

Within PIMC, the quantum system of N particles is mapped onto a classical system of N ring-polymers.[31] Each ring-polymer is composed of beads, whose number is fixed by expressing the full density matrix $\rho(R,R',T) = \langle R|\exp(-\hat{H}/k_BT)|R'\rangle$ ($\hat{H}$ is the Hamilton operator, R and

R' are many-body coordinates representing the positions of the N particles, and T is the temperature), via a Trotter decomposition, as a convolution of higher temperature density matrices $\rho(R,R',T')$. In our simulations, we adopted the pair-Suzuki approximation[32] for $\rho(R,R',T')$ with $T' = 720$ K and assumed a total number of 54 and 41 convolutions for the pH_2-Ne and oD_2-Ne systems, respectively. The corresponding temperatures are $T = 13.09$ K and $T = 17.14$ K, respectively, which represent the estimated experimental average filament temperatures of the pure systems;[12] given the low Ne content, the same temperatures have been assumed also for the simulations of the mixtures.

To determine the geometry of the local environment (either crystalline or liquid) around a particular particle of the simulated quantum binary mixtures, we used the identification schema based on the LBO parameters introduced by Steinhardt *et al.*,[33] modified by averaging the LBO parameters over the nearest neighbors of the analyzed particle and the particle itself.[34] Since quantum delocalization invariably leads to large fluctuations in the beads' positions, thereby deteriorating the LBO analysis, the LBO parameters were computed by using the centre of mass of each ring-polymer as the particle position.[35] In addition, in order to guarantee a univocal choice of the nearest neighbors of a given particle, we employed a three dimensional Delaunay triangulation. The averaged LBO parameters were then used to define different coarse-grained rotationally invariant parameters that are sensitive to different spatial symmetries.[34] For example, the invariant Q_6 is ideally suited to distinguish between the crystalline and disordered liquid-like configurations, whereas the invariant Q_4 allows distinguishing between different types of crystal structures. Conversely, one can construct the invariant w_6 that we used to analyze the tendency of the simulated systems to develop icosahedral-like structures.[36]

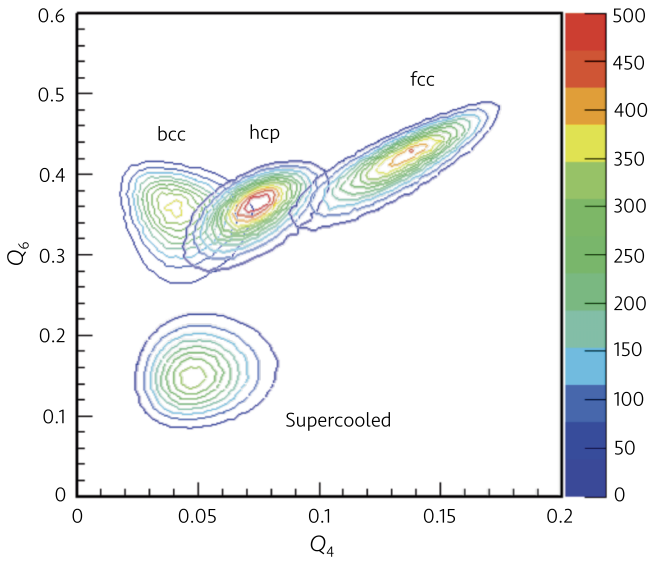

FIG. 8. Contour plots of the computed probability distributions $p(Q_4,Q_6)$ for pH_2 simulated in the bcc, hcp, and fcc crystal phases at $T \simeq 12$ K and $\rho = 0.0240$ Å^{-3} and in a metastable liquid state at $T \simeq 13$ K and $\rho = 0.0232$ Å^{-3}. Note that the use of periodic boundary conditions compatible with a specific crystal lattice allows simulating also crystalline states different from the equilibrium hcp solid phase of pH_2.

In order to prevent the crystallization of the mixtures during our PIMC simulations, we adopted different strategies. We used a number of particles and a simulation box with side-ratios non-compatible with close-packed crystal lattices; moreover, we generated the starting disordered configuration for our simulations as reported in Ref. 37. The validity of our choices has been checked by computing the probability distributions $p(Q_4,Q_6)$ for the ordered and disordered configurations, shown in Fig. 8 for a pure pH_2 system;[12] the probability distribution for disordered supercooled liquid pH_2 is clearly well separated from the distributions computed for different crystal lattices, indicating the absence of any sign of crystallization in the configurations sampled for the metastable system. Similar results have been obtained for all the quantum binary mixtures considered in the present study.

[1]M. D. Ediger and P. Harrowell, J. Chem. Phys. **137**, 080901 (2012).
[2]M. D. Ediger, P. Harrowell, and L. Yiu, J. Chem. Phys. **128**, 034709 (2008).
[3]M. L. F. Nascimento and E. D. Zanotto, J. Chem. Phys. **133**, 174701 (2010).
[4]C. Tang and P. Harrowell, Nat. Mater. **12**, 507 (2013).
[5]J. Orava and A. L. Greer, J. Chem. Phys. **140**, 214504 (2014).
[6]D. Wang, Y. Li, B. B. Sun, M. L. Sui, K. Lu, and E. Ma, Appl. Phys. Lett. **84**, 4029 (2004).
[7]J. R. Fernández and P. Harrowell, Phys. Rev. E **67**, 011403 (2003).
[8]D. Coslovich and G. Pastore, J. Chem. Phys. **127**, 124504 (2007).
[9]L.-C. Valdes, F. Affouard, M. Descamps, and J. Habasaki, J. Chem. Phys. **130**, 154505 (2009).
[10]A. Banerjee, S. Chakrabarty, and S. M. Bhattacharyya, J. Chem. Phys. **139**, 104501 (2013).
[11]M. Kühnel, J. M. Fernández, G. Tejeda, A. Kalinin, S. Montero, and R. E. Grisenti, Phys. Rev. Lett. **106**, 245301 (2011).
[12]M. Kühnel, J. M. Fernández, F. Tramonto, G. Tejeda, E. Moreno, A. Kalinin, S. Montero, D. E. Galli, and R. E. Grisenti, Phys. Rev. B **89**, 180201(R) (2014).
[13]I. F. Silvera, Rev. Mod. Phys. **52**, 393 (1980).
[14]S. R. Williams, C. P. Royall, and G. Bryant, Phys. Rev. Lett. **100**, 225502 (2008).
[15]S. R. Challa and J. K. Johnson, J. Chem. Phys. **111**, 724 (1999).
[16]J. M. Fernández, M. Kühnel, G. Tejeda, A. Kalinin, R. E. Grisenti, and S. Montero, AIP Conf. Proc. **1501**, 1296 (2012).
[17]J. P. Brouwer, C. J. N. Van Den Meijdenberg, and J. J. M. Beenakker, Physica **50**, 93 (1970).
[18]A. S. Baryl'nik, A. I. Prokhvatilov, M. A. Strzhemechnyĭ, and G. N. Shcherbakov, Low Temp. Phys. **19**, 447 (1993).
[19]N. N. Gal'tsov, A. I. Prokhvatilov, and M. A. Strzhemechnyĭ, Low Temp. Phys. **30**, 984 (2004).
[20]V. G. Belan, N. N. Galtsov, A. I. Prokhvatilov, and M. A. Strzhemechnyĭ, Low Temp. Phys. **31**, 947 (2005).
[21]B. J. Kozioziemski and G. W. Collins, Phys. Rev. B **67**, 174101 (2003).
[22]J. V. Kranendonk, *Solid Hydrogen* (Plenum, New York, 1983).
[23]K. A. Jackson, Interface Sci. **10**, 159 (2002).
[24]C. P. Royall and S. R. Williams, Phys. Rep. **560**, 1 (2015).
[25]S. Stüber, D. Holland-Moritz, T. Unruh, and A. Meyer, Phys. Rev. B **81**, 024204 (2010).
[26]P. Kuhn, J. Horbach, F. Kargl, A. Meyer, and Th. Voigtmann, Phys. Rev. B **90**, 024309 (2014).
[27]A. B. Hopkins, F. H. Stillinger, and S. Torquato, Phys. Rev. E **85**, 021130 (2012).
[28]A. Hirata, L. J. Kang, T. Fujita, B. Klumov, K. Matsue, M. Kotani, A. R. Yavari, and M. W. Chen, Science **341**, 376 (2013).
[29]M. Guerdane, H. Teichler, and B. Nestler, Phys. Rev. Lett. **110**, 086105 (2013).
[30]I. F. Silvera and V. V. Goldman, J. Chem. Phys. **69**, 4209 (1978).
[31]D. M. Ceperley, Rev. Mod. Phys. **67**, 279 (1995).
[32]M. Rossi, M. Nava, L. Reatto, and D. E. Galli, J. Chem. Phys. **131**, 154108 (2009).
[33]P. Steinhardt, D. R. Nelson, and M. Ronchetti, Phys. Rev. B **28**, 784 (1983).
[34]W. Lechner and C. Dellago, J. Chem. Phys. **129**, 114707 (2008).
[35]M. Rossi, E. Vitali, L. Reatto, and D. E. Galli, Phys. Rev. B **85**, 014525 (2012).
[36]M. Leocmach and H. Tanaka, Nat. Commun. **3**, 974 (2012).
[37]O. N. Osychenko, R. Rota, and J. Boronat, Phys. Rev. B **85**, 224513 (2012).